International Journal of Thermal Sciences 110 (2016) 251–260

Contents lists available at ScienceDirect

International Journal of Thermal Sciences

journal homepage: www.elsevier.com/locate/ijts

Probing horizontal convection instability via perturbation of the forcing boundary layer using a synthetic jet

Matthew A. Leigh, Tzekih Tsai, Gregory J. Sheard*

The Sheard Lab, Department of Mechanical and Aerospace Engineering, Monash University, VIC 3800, Australia

ARTICLE INFO

Article history:
Received 1 February 2016
Received in revised form
27 May 2016
Accepted 18 July 2016

Keywords:
Horizontal convection
Nusselt number
Boundary-layer instability
Synthetic jet

ABSTRACT

Horizontal convection driven by a linear temperature profile along the bottom of a two-dimensional rectangular enclosure is perturbed by a small tuned synthetic (zero-net-mass-flux/ZNMF) jet. The jet permits instability in the horizontal convection boundary layer to be investigated in a controlled manner. At a Prandtl number $Pr = 6.14$ and Rayleigh number $Ra = 2.5 \times 10^8$, slightly below the natural onset of instability, the boundary layer is found to be convectively unstable, exhibiting a disturbance pattern consistent with a Rayleigh–Bénard mechanism. Advection of the boundary layer disturbance gives rise to unsteadiness in the vertical end-wall plume. Nusselt number is enhanced across a range of frequencies for all perturbation amplitudes, with the response dominated by two frequencies differing by approximately a factor of two: each invokes the periodic shedding of vorticity into the vertical end-wall plume at the higher frequency. This suggests that there exists a natural sensitivity in this flow to disturbances convecting in the upstream boundary layer. That is, a convective instability in the horizontal convection boundary layer serves as a disturbance amplifier, with the end-wall plume controlling the frequency of the resulting instability mode. The increase in Nusselt number achieved by a jet with peak speed of the same order as the horizontal convective velocity in the unperturbed flow is consistent with a greater than two-fold increase in Rayleigh number.

1. Introduction

Horizontal convection is a form of convection in which the flow is triggered by a heating differential applied across one horizontal boundary, which can be either the top or bottom boundary in an enclosure. Unlike the comprehensively studied Rayleigh–Bénard convection, in which vertical heating from below promotes instability beyond some critical Rayleigh number, in horizontal convection the non-uniform heating over the forcing boundary leads to overturning of the fluid for all Rayleigh numbers [1]. Horizontal temperature gradients are found in myriad geophysical flows, including the Earth's oceans, atmosphere and mantle [2], though it is the oceanographic application towards the global thermocline current system that has motivated significant recent attention to horizontal convection [1,3–9].

The characteristics of horizontal convection are highly dependent on the Rayleigh number, which indicates the strength of the applied heating differential. Fluid flow at low Rayleigh numbers is laminar and diffusive in nature; and no boundary layer is present. In this regime, overturning circulation is approximately symmetrical and is caused by the destabilizing buoyancy input. At higher Rayleigh numbers the fluid flow moves from a diffusion-dominated to a convection-dominated behaviour, where thermal and velocity boundary layers establish along the horizontal boundary on which the differential temperature is applied [5].

At Prandtl numbers consistent with water, horizontal convection flow becomes time-dependent beyond a critical Rayleigh number [3,5]. Instability presents initially as a convecting transverse-roll wave in the forcing boundary layer along with a time-periodic pulsing in the end-wall plume. This soon gives way to an eruption of mushroom shaped plumes breaking out from the boundary layer and rising near the end-wall as a vertical plume. The plume transports the hotter, more buoyant fluid towards the top of the tank, before it recirculates horizontally along the top and diffuses in the interior of the box. Understanding the nature of the instabilities in horizontal convection is important as controversy remains regarding both the transition to unstable flow and the role of turbulence in the flow. Paparella and Young [10] proved for horizontal convection that in the limit of vanishing thermal and

* Corresponding author.
E-mail address: greg.sheard@monash.edu (G.J. Sheard).

http://dx.doi.org/10.1016/j.ijthermalsci.2016.07.007
1290-0729/

Nomenclature

A	synthetic jet peak velocity amplitude
c_p	fluid specific heat capacity
d	jet orifice width
$\widehat{\boldsymbol{e}}_y$	unit vector in y-direction
f	frequency
f_j	synthetic jet frequency
F_T	absolute base heat flux
g	gravitational acceleration
H	enclosure height
L	enclosure width
N_p	element polynomial degree
Nu	nusselt number
p	pressure
Pr	prandtl number
Ra	rayleigh number
t	Time
T	time period
$\boldsymbol{u}$	velocity vector
v_j	synthetic jet vertical velocity
x	cartesian horizontal coordinate
x_j	horizontal jet position
ZNMF	zero-net-mass-flux

Greek symbols

α	volumetric expansion coefficient
$\delta\theta$	horizontal temperature difference across base
θ	temperature
θ_0	reference temperature
κ_T	fluid thermal diffusivity
ν	fluid kinematic viscosity
ρ_0	fluid density
ω_z	spanwise vorticity

molecular dissipation for fixed Prandtl number, that the energy dissipation per unit mass also vanishes. Horizontal convection therefore does not satisfy the *law of finite energy dissipation* (the 'zeroth law of turbulence), and is therefore formally non-turbulent. It does, though, exhibit some features consistent with a turbulent flow. Fig. 3 in Ref. [10] demonstrates unsteady and time-dependent features, which have also been observed in subsequent experimental and numerical studies [3,5,8,11], along with evidence of a spectral cascade [8].

The development of instability in horizontal convection has been linked to a possible increase in the scaling of Nusselt number characterising heat transport with Rayleigh number from the laminar scaling developed by Rossby [12], $Nu \sim Ra^{1/5}$ [3,5,8,13]. The scaling of horizontal convection with Rayleigh number has also been studied recently by Ilıcak and Vallis [14] and Hazewinkel et al. [15]. A theoretical upper bound of $Nu \sim Ra^{1/3}$ has been proposed [16] but has yet to be observed. The ultimate value of the scaling exponent at high Rayleigh numbers may have significant implications for the contribution of horizontal convection to global overturning and heat transport in Earth's oceans, and so is of significant interest. Indeed, a recent theoretical consideration of heat and momentum dissipation in the boundary layer and interior of horizontal convection following the ideas of Grossmann and Lohse [17] led to the development of a sketch of the horizontal convection scaling regimes in Pr–Ra space [18]. At high Rayleigh numbers their theory predicts both a $Ra^{1/4}$ regime and the upper-bound $Ra^{1/3}$ regime at higher and lower Prandtl numbers, respectively; both regimes exceed Rossby's $Ra^{1/5}$ scaling.

While the manifestation of instability in horizontal convection is increasingly well understood [1,5,8], the characteristics of the underlying instability mechanism are less clear. The onset of unsteady flow has been attributed to a pulsing in the end-wall plume [6], though recent simulations [5,8] have also demonstrated convecting two-dimensional disturbances within the forcing boundary layer upstream of the plume. Tsai et al. [19] demonstrated using a one-dimensional linear stability analysis that these disturbances arise from a Rayleigh–Bénard type of thermal instability mechanism at the hotter end of the bottom boundary. The precise connection between these disturbances and their respective contributions to the development of unsteady flow in horizontal convection remains unknown. This study proceeds on the hypothesis that instability originates within the forcing boundary layer, and seeks to investigate the response of the flow at a Rayleigh number just below the natural onset of instability to a controlled, localised perturbation of the boundary layer.

In 1948, Schubauer and Skramstad [20] published a landmark report into the stability of laminar boundary layers. They mounted a vibrating ribbon within a stable boundary layer, and by controlling the amplitude and frequency of the vibration, were able to map the stability of the boundary layer using measurements of the response of the flow to the applied perturbation. A similar methodology is adopted in this study, though for numerical convenience a synthetic jet located on the forcing boundary is employed in place of a vibrating ribbon to perturb the boundary layer. Synthetic, or zero-net-mass-flux (ZNMF), jets are a type of jet flow generated by cyclic movement of fluid into and out of a small opening [21]. They have the distinguishing property when compared to other jet flows that the jet is composed only of the surrounding fluid (there is no net injection of fluid from an external source). Synthetic jets find important application as actuators for aerodynamic flow control [22,23], including control of flow separation [24] and study of turbulent transition [25,26].

The addition of the synthetic jet places this study within the domain of mechanically forced horizontal convection. In Hazewinkel et al. [15], simulations of horizontal convection with a time invariant shear stress applied over the breadth of the heated boundary was considered. In their study the mechanical forcing was 'thermally indirect,' acting in opposition to the direction of overturning due to the buoyancy forcing. They recalled Sandstr om's [27] observation of wind reversing the direction of surface flow in a fjord in western Sweden, and primarily reported on the ability of opposing surface shear stress to establish a regime featuring a shallow thermally indirect shear-driven overturning cell near the forcing boundary, beyond which lay a larger thermally direct buoyancy-driven cell. Tailleux and Rouleau [28] considered a square enclosure ($H/L = 1$) with a linear temperature profile applied over the top surface, and mechanical forcing applied as a vorticity source spanning 1/3 of the enclosure depth and 1/2 the enclosure width, extending from the upstream end of the heated boundary. In contrast to [15], the mechanical forcing configuration was localised rather than spanning the forcing boundary, and was imposed in both direct (acting with the buoyancy forcing) and indirect (opposing the buoyancy forcing) configurations. They concluded that mechanical forcing enhances horizontal convection by increasing the energy extracted from the buoyancy forcing, enhancing mixing, increasing the thermocline depth and production rate of available potential energy. Ilıcak and Vallis [14] considered a horizontal convection system with a buoyancy

profile applied across the top boundary such that a central descending plume was invoked, with return flows towards the left and right of the enclosure. They invoked a mechanical forcing via imposition of a uniform vorticity across the top boundary that varied sinusoidally in time about zero. Hence their configuration imposed no net forcing acting in cooperation or opposition to the natural buoyancy-driven overturning flow. This property is shared with the configuration adopted in the present study, though here the perturbation is added via a localised synthetic jet, specifically positioned at the upstream end of the convectively unstable part of the boundary layer at the chosen flow conditions.

This paper is structured as follows: § 2 defines the problem setup, governing equations and numerical formulation, § 3 describes the results, which includes a description of the unperturbed reference flow, the response of Nusselt number to the applied perturbation, and elucidation of the response through interrogation of thermal and disturbance fields. Finally, conclusions are drawn in § 4.

2. Numerical model and methodology

2.1. Model description

Fig. 1 shows a schematic diagram of the problem being investigated. The system consists of a two-dimensional fluid undergoing horizontal convection in a rectangular box with height H and width L. Consistent with several previous studies [3,5,8], a fixed enclosure aspect ratio of $H/L = 0.16$ is used. The flow is driven by a linear temperature profile applied along the base of the enclosure. The remaining three walls are perfectly insulated. The imposition of a fixed temperature distribution across the jet orifice ensures that no net advective heat flux is created by the addition of the jet. The two side walls have a no-slip velocity boundary condition imposed. The bottom surface has a no-slip boundary condition, with the exception of the synthetic jet location, while the upper horizontal boundary features a second broad and weak synthetic jet to satisfy conservation of mass. The parameters quantifying the applied perturbation include the synthetic jet peak velocity amplitude A, oscillation frequency f_j, horizontal position of the centre of the jet along the base x_j, and orifice width d. This work seeks to characterise the response of the flow via the Nusselt number to boundary-layer perturbation of specific amplitude and frequency.

2.2. Governing equations and parameters

The governing equations are the dimensionless Navier–Stokes equations for a Boussinesq fluid, which are expressed as

$$\nabla \cdot \boldsymbol{u} = 0, \tag{1}$$

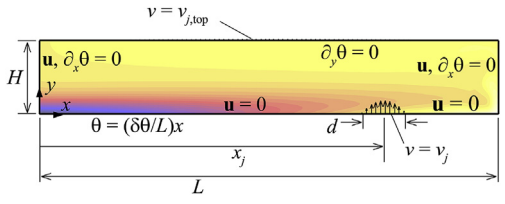

Fig. 1. Schematic representation of the two-dimensional problem under consideration. Enclosure dimensions and boundary conditions on velocity and temperature fields are labelled. The abbreviation ∂_x represents the partial derivative with respect to x, the synthetic jet velocity profile v_j is defined in Eqn. (4), and mass is conserved by prescribing a weak complementary vertical flow ($v_{j,\mathrm{top}}$) through the top boundary.

$$\frac{\partial \boldsymbol{u}}{\partial t} = -(\boldsymbol{u}\cdot\nabla)\,\boldsymbol{u} - \nabla p + Pr\,\nabla^2\boldsymbol{u} + PrRa\,\hat{\boldsymbol{e}}_y\,\theta, \tag{2}$$

$$\frac{\partial \theta}{\partial t} = -(\boldsymbol{u}\cdot\nabla)\,\theta + \nabla^2\theta, \tag{3}$$

where $\boldsymbol{u}$, t, p, Pr, Ra, $\hat{\boldsymbol{e}}_y$ and θ are the velocity vector, time, kinematic static pressure, Prandtl number, Rayleigh number, unit vector in the upward vertical direction, and temperature, respectively. Length, velocity, time, pressure and temperature are respectively scaled by L, κ_T/L, L^2/κ_T, $\rho_0\kappa_T^2/L^2$ and $\delta\theta$, where κ_T and ρ_0 are the thermal diffusivity and reference density of the working fluid, and $\delta\theta$ is the imposed temperature difference across the bottom boundary. Temperature is taken relative to a reference temperature θ_0 such that the absolute temperature is recovered from $\theta + \theta_0$. The reference temperature is arbitrarily taken as the temperature at the cold end of the heated boundary. Hereafter, these quantities are expressed in their normalised form.

The Rayleigh number, which characterizes the strength of thermal forcing, is defined as $Ra = \alpha g\,\delta\theta\,L^3/\nu\kappa_T$, where g is the acceleration due to gravity, α the volumetric thermal expansion coefficient, and ν the kinematic viscosity of the fluid.

Previous studies have determined for horizontal convection in an enclosure forced by a linear temperature profile (as used here) that the flow transitions from a steady convective state to a state exhibiting a time-periodic instability beyond $Ra \approx 5 \times 10^8$ [5]. As our interest is in the mechanisms underpinning this primary instability in horizontal convection, we consider the flow at $Ra = 2.5 \times 10^8$, slightly below the onset of the transition.

The two-dimensional approach taken here is justified by the observation from high-resolution three-dimensional direct numerical simulation by Gayen et al. [8]. Those observations are in turn supported by the linear stability analysis of Tsai et al. [19], where the horizontal convection boundary layers were found to first become unstable to transverse-roll (two-dimensional) disturbances with increasing Rayleigh number, prior to the onset of longitudinal-roll (three-dimensional) instability.

The Prandtl number $Pr = \nu/\kappa_T$, characterizes the ratio of viscous to thermal dissipation in the fluid, and consistent with water at room temperature, $Pr = 6.14$ is used in this study.

The Nusselt number, which is the ratio of convective to conductive heat transfer, is defined as $Nu = F_T L/\rho_0 c_p \kappa_T \delta\theta$, where here we take F_T as the time average of the absolute value of the heat flux averaged over the forcing boundary, and c_p is the specific heat capacity of the fluid.

The forcing boundary layer is perturbed by a small synthetic jet embedded in the forcing boundary. This study is concerned with the response of the flow to the applied perturbation rather than the local flow dynamics in the vicinity of the jet orifice, so for simplicity the jet is modeled by an oscillatory parabolic velocity profile described by

$$v_j = A\left[1 - \frac{4}{d^2}(x - x_j)^2\right]\sin\left(2\pi f_j\, t\right). \tag{4}$$

The velocity v_j is applied over $x_j - d/2 \le x \le x_j + d/2$, $t \ge 0$. A jet position of $x_j = 0.75L$ and width of $d = 0.1$ are used throughout this analysis. This position was chosen to correspond to the inception of convective instability in the forcing boundary at $Ra = 2.5 \times 10^8$ following [29,19].

Peak jet velocity amplitudes up to $A = 1000$ are considered in this study. At this amplitude the peak jet flow rate is of the same order as the horizontal flow speed within the kinematic forcing boundary layer above the jet. Our interest is in perturbation of the

boundary layer rather than its destruction, so larger amplitudes are not considered.

2.3. Numerical method

The governing equations are solved numerically using a high-order solver implementing a spectral element method for spatial discretisation and a third-order time integration scheme based on backwards differentiation. The solver has been validated and employed extensively for heat transport [30] and natural convection flows [5,9,31]. The spectral element method combines the desirable convergence properties of the spectral method and the geometric flexibility of the finite element method [32]. An operator-splitting approach [33] is taken to advance the velocity and thermal fields in time. The advection terms are treated explicitly, with fields projected to the future time using polynomial extrapolation for evaluation of the first term on the right-hand side of each of equations (2) and (3). The convection (or non-conservative) form of the discrete advection operators are used, which requires fewer operations to compute and demonstrates superior convergence with increasing spectral order to the formally conservative alternatives such as the skew-symmetric or rotational forms [34,35]. The buoyancy contribution is also calculated at this step. A Poisson equation for pressure is then constructed to project the velocity field onto a divergence-free space, satisfying (1). Finally, a set of Helmholtz equations are constructed from the viscous and thermal diffusion terms to implicitly solve for the final velocity and thermal fields. Dirichlet boundary conditions for velocity and temperature are strongly enforced at this step, while Neumann boundary conditions are weakly enforced. A mesh consisting of 3692 rectangular elements with a coarser mesh in the centre of the domain and higher element density in close proximity to the boundaries to resolve the boundary layers was used.

2.4. Grid independence

To assess the resolution required to reduce spatial discretisation errors to within an acceptable level, convergence with increasing element polynomial degree N_p of each of the mean temperature θ_{avg} over the flow domain, the $\mathscr{L}^2$ norm of the velocity field, and the contributions to the Nusselt number over the colder Nu_{cold} and hotter Nu_{hot} halves of the heated boundary were monitored for an unperturbed case having $Ra = 2.5 \times 10^8$, $Pr = 6.14$ and $H/L = 0.16$. The results of this convergence study are shown in Fig. 2. The percentage error at each N_p is taken relative to the next higher-resolution case, i.e. $N_p + 1$. Error in the $\mathscr{L}^2$ norm decreases rapidly to less than $\mathscr{O}(10^{-7}\%)$ by $N_p = 7$. Errors in θ_{avg} and Nu_{hot} floor out by $N_p = 8$ with errors less than $\mathscr{O}(10^{-6}\%)$. The error in Nu_{cold} similarly rapidly reduces with increasing N_p up to $N_p = 6$, but poor convergence is seen thereafter. By $N_p = 6$, the errors across these quantities are already very small, ranging between $\mathscr{O}(10^{-7}\%)$ and $\mathscr{O}(10^{-4}\%)$, and up to this resolution the percentage errors decrease approximately exponentially with increasing N_p, which is a desirable property of the spectral element method [32]. Therefore a polynomial degree $N_p = 6$ is used hereafter. Additionally, at this resolution the error in mass conservation due to finite resolution of the two jet profiles was a negligible $7.38 \times 10^{-7}\%$.

The modest convergence performance beyond $N_p = 6$ of the Nu_{cold} quantity was investigated, and is believed to be due to the sign change in wall heat flux between the regions of cooling and heating along the base. At this Rayleigh number this sign-change occurs just to the left of the half-way point (at $x \approx 0.47$), which lies within the cooler half of the base. As our Nusselt number is calculated from the *absolute value* of heat flux averaged over the heated boundary, this change in sign creates a discontinuity in the gradient of the absolute heat flux distribution $|\partial\theta/\partial y|$ with respect to x. This non-smooth variation renders the high-order polynomial shape functions within the spectral elements susceptible to Runge's phenomenon (spurious oscillations in a polynomial interpolant), which explains the erosion in the quality of the convergence of Nu_{cold} with increasing polynomial order. The hotter half of the base has no such sign change in $\partial\theta/\partial y$ and correspondingly exhibits significantly superior convergence.

2.5. Verification of heat conservation

Conservation of heat by the solver will now be considered. The heat transport equation (3) can be recast in integral form for application to a control volume containing the enclosure as

$$\frac{\partial}{\partial t}\iiint_{\Omega}\theta \,\mathrm{d}\Omega = -\oiint_{\Gamma}\theta\, \boldsymbol{u}\cdot\boldsymbol{n}\,\mathrm{d}\Gamma + \oiint_{\Gamma}\nabla\theta\cdot\boldsymbol{n}\,\mathrm{d}\Gamma, \tag{5}$$

where Ω and Γ are respectively the computational domain and its boundaries, and $\boldsymbol{n}$ is a outward normal unit vector. The term on the left-hand side describes the rate of change of heat in the enclosure. This is balanced by the terms on the right-hand side, which

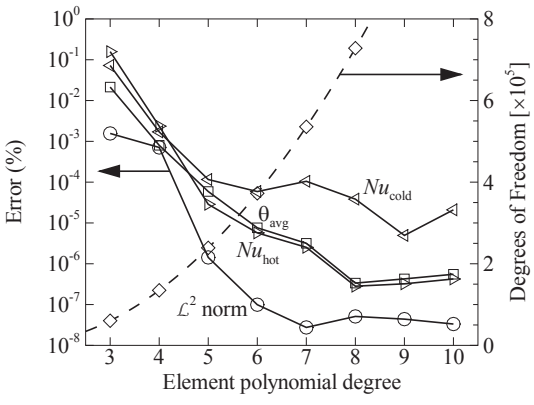

Fig. 2. Percentage errors in $\mathscr{L}^2$ norm (○), average temperature θ_{avg} (□), and the contributions to Nusselt number over the cooler and hotter halves of the base, Nu_{cold} (◁) and Nu_{hot} (▷), respectively, for the unperturbed case ($Ra = 2.5 \times 10^8$, $Pr = 6.14$ and $H/L = 0.16$). The number of degrees of freedom at each polynomial degree is also displayed (dashed line), and lines connecting each point are added for guidance.

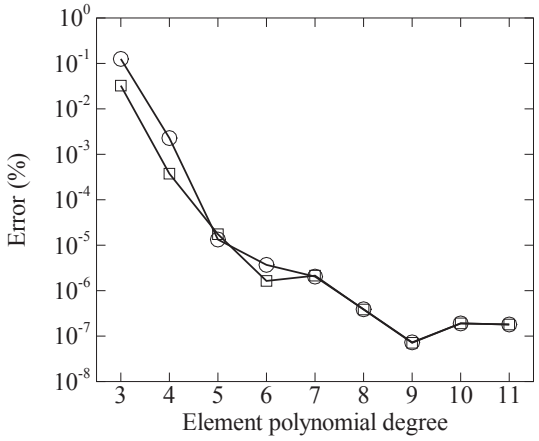

Fig. 3. Conservation of heat at steady-state for the unperturbed reference case with $Ra = 2.5 \times 10^8$, $Pr = 6.14$ and $H/L = 0.16$. Net heat flux out of the enclosure (□) and net heat flux through the bottom boundary (○) expressed as percentages of the total absolute heat flux across the base. Lines connecting each point are added for guidance.

respectively describe heat flux due to advection and conduction across the enclosure boundaries. For the unperturbed reference case the first term on the right-hand side is always zero as there is no flow through any of the enclosure boundaries. The second term will also be zero on the thermally insulated top and size boundaries. Along the bottom boundary, the second term may be non-zero if conductive heating and cooling are not in balance. At thermal equilibrium, horizontal convection is well-known to have no net vertical heating across any horizontal plane [1]. Hence heating and cooling through the bottom boundary must be in balance and the second term in (5) must sum to zero.

The reference case considered in this study (having $Ra = 2.5 \times 10^8$, $Pr = 6.14$ and $H/L = 0.16$) is time-invariant at thermal equilibrium. Hence each term in equation (5) should be zero. However, the present solver adopts a weak enforcement of Neumann boundary conditions (such as the zero thermal gradient for insulating boundaries) through the Galerkin treatment of the elliptic problem constructed to implicitly solve the diffusion term in equation (3). Thermal insulation is therefore inexactly enforced by the solver, so it is pertinent to quantify the error in heat conservation by the present scheme. Fig. 3 plots both the total conductive heat flux through all boundaries (the last term in equation (5)) and along the bottom boundary as percentages of the total heat flux magnitude, against element polynomial degree for the reference case at thermal equilibrium. Both of these quantities should be zero at thermal equilibrium and so non-zero values can be interpreted as heat conservation errors by the solver; the plot demonstrates that these errors decrease from $\mathscr{O}(10^{-1}\%)$ at $N_p = 3$ to $\mathscr{O}(10^{-6}\%)$ at $N_p = 6$. This confirms that the solver reliably conserves heat at the selected resolution $N_p = 6$.

The advection of fluid at the jet orifice and compensatory top boundary admits the possibility of non-zero contributions of the first term on the right-hand side of equation (5) as the integrand product $\theta \boldsymbol{u}$ can be non-zero at these locations. The imposition of a fixed temperature at the jet orifice ensures that the jet adds no net advective heat flux due to its zero net flow. However, there remains the possibility of non-zero net advective heat flux through the top boundary as the temperature is not fixed at this boundary. While any such net heat flux would be balanced by additional heat conduction through the bottom boundary at thermal equilibrium, such a condition would introduce a net vertical heat flux through the enclosure that is normally absent from unperturbed horizontal convection [1]. A test case is computed at $Ra = 2.5 \times 10^8$, $Pr = 6.14$, $H/L = 0.16$ with synthetic jet amplitude $A = 32$ and oscillation frequency $f_j = 4000$ to a statistically steady state. A segment of the time history at this equilibrium state is shown in Fig. 4, where the time-variation of each of the integral terms in equation (5) are plotted. As a percentage of the time mean absolute value of conductive heat flux through the bottom boundary, the net vertical heat flux through the base is a negligible $7.5 \times 10^{-5}\%$. Hence despite the activation of the synthetic jet, the system retains the zero net vertical heat transport consistent with unperturbed horizontal convection.

3. Results and discussion

3.1. Baseline case

In this section, the flow case with no applied perturbation is considered, which sets the framework for the subsequent sections. It should be emphasized that the flow in the current configuration is stable: this baseline case is for a Rayleigh number of 2.5×10^8, which is below the critical Rayleigh number of approximately 5×10^8 [5]. This is important as it isolates the effect of the synthetic jet on the flow instability.

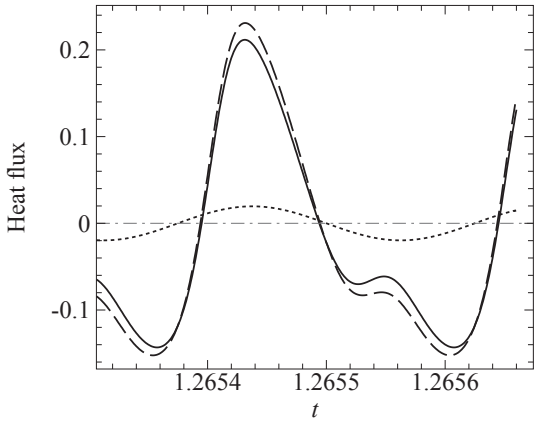

Fig. 4. Demonstration of heat balance for a perturbed case with jet amplitude $A = 32$ and frequency $f_j = 4000$. The unbroken curve shows the total heat flux due to conduction out of all boundaries (the last term in equation (5)), the dashed curve shows the rate of change of temperature within the enclosure (the left-hand side of equation (5); calculated using second-order centred differences from data acquired at 250 samples per jet oscillation period). The dotted curve plots the difference between the aforementioned quantities, which corresponds to the total heat flux due to convection out of all boundaries (the first term on the right-hand side of equation (5)). A segment of the time-history of these quantities is shown when the fluid and heat flow are at statistical steady state.

Plots of the two-dimensional steady-state temperature and vorticity fields for the baseline case are shown in Fig. 5. Guidance lines identify the forcing thermal and kinematic boundary layers, and it is seen that at this Rayleigh number a strong convection-dominated flow has established. The thermal boundary layer begins to form at approximately $x = 0.4$, while the velocity boundary layer originates at the bottom-left corner ($x = 0$). The velocity boundary layer is thinner than the corresponding thermal boundary layer, however the thickness of both boundary layers continue to grow in size as the flow approaches the hotter end ($x \to 1$). The flow is steady-state, confirming that this model correctly captures the stable solution of the flow at this Rayleigh and Prandtl number. A region of strong positive vorticity is seen close to the right hand wall of the domain, which is the early formation of a vertical plume that transports the heated flow towards the top of the enclosure

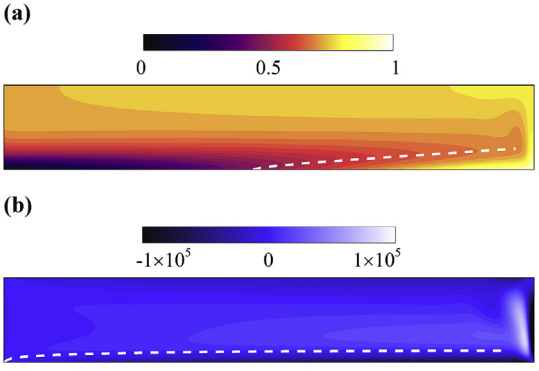

Fig. 5. The steady-state two-dimensional solution computed at $Ra = 2.5 \times 10^8$, $Pr = 6.14$ and $H/L = 0.16$. (a) Temperature field: dark to light contours are equispaced between the coldest and hottest temperatures in the enclosure, $0 \leq \theta \leq 1$, and the dashed line identifies the edge of the thermal boundary layer (taken as the location of minimum temperature vertically from the bottom wall). (b) Vorticity field: dark and light contours show negative and positive vorticity over $-1 \times 10^5 \leq \omega_z \leq 1 \times 10^5$, where vorticity ω_z is normalised by κ_T/L^2, and the dashed line identifies the edge of the kinematic boundary layer (taken as the first zero-vorticity - and hence maximum horizontal velocity - location vertically from the bottom wall).

before it diffuses into the remainder of the domain. The requirement of zero net heating across any horizontal plane at equilibrium [1] helps to explain the slow and broad downwelling across the cooler region of the enclosure that leads to the highly asymmetric flow seen here [12]. This baseline case serves as a reference point for the remainder of this study; in the following sections the addition of the synthetic jet and its effect on the flow are elucidated.

3.2. Nusselt number response of the flow to perturbation amplitude and frequency variation

The Nusselt number is employed to assess the response of the flow to the applied perturbation. This is motivated by the observed increase in Nusselt number associated with the onset of instability reported in recent studies [5,8]. The jet frequency dependence of Nusselt number at different jet amplitudes is plotted in Fig. 6. Jet amplitudes $A < 1$ generate a negligible change in Nusselt number from the $A = 0$ baseline: at $A = 1$ the maximum deviation from the reference Nusselt number was a mere 0.08% increase. $A = 10$ produced an observable increase in Nu over a frequency band $5 \times 10^3 \lesssim f_j \lesssim 10^4$, with a peak at $f_j = 7.47 \times 10^3$. The flow characteristics arising from these jet perturbations leading to elevated Nu will be explored in § 3.3–3.5. Further increases in A widen the range of frequencies at which elevated Nu is found, and increase the maximum Nu in the excited frequency band. Nevertheless, all explored cases ($A \leq 1000$) produce a monotonic decrease in Nu down towards the reference value as $f_j \to \infty$. Two distinct Nusselt number maxima are evident within the excited frequency range. The aforementioned local maximum in Nusselt number is achieved at frequencies $f_j \approx 7.5 \times 10^3$ (hereafter referred to as the HF mode), and is captured at smaller amplitudes ($A \lesssim 100$). A second local maximum at $f_j \approx 4000$ appears across all amplitudes (hereafter the LF mode). The LF mode produces a smaller increase in Nu than the HF mode at amplitudes $A \lesssim 32$, but it exhibits strong growth in Nu at higher amplitudes, surpassing the HF mode peak at $A = \mathcal{O}(10^2)$. By $A = 320$, the HF mode maximum has been absorbed by the LF mode.

At $A = 1000$, the peak enhancement in Nusselt number is 16.7%. Under Rossby's $Nu \sim Ra^{1/5}$ scaling (valid in this Rayleigh number regime [5,8]), an unperturbed horizontal convection flow would require a greater than twofold increase in Rayleigh number (a factor of 2.16) to produce this higher rate of convective heat transport. At the reference conditions ($Ra = 2.5 \times 10^8$, $Pr = 6.14$, $H/L = 0.16$), the maximum horizontal velocity is approximately 8.2×10^2, which occurs within the boundary layer adjacent to the heated boundary

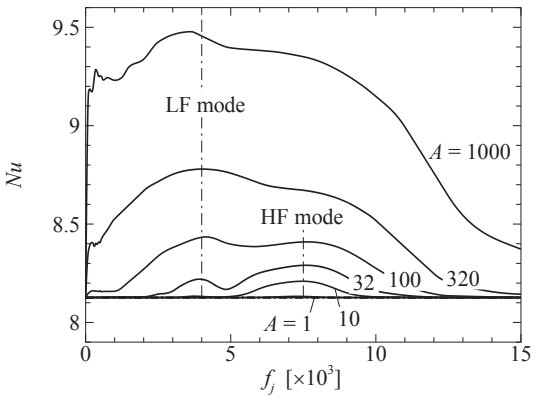

Fig. 6. Nusselt number plotted against jet frequency for jet amplitudes as shown. Akima splines have been fitted to the data for guidance.

towards the hot end of the enclosure. It is therefore found that a localised perturbation with velocities only of the same order as the horizontal convective transport velocity can destabilise the horizontal convection flow so profoundly as to produce an elevation in heat transport consistent with *greater than a doubling* of the strength of thermal forcing across the horizontal boundary. This may have implications for future consideration of the importance of localised wind stresses to buoyancy driven overturning in the oceans.

The Nusselt numbers of the perturbed flows in Fig. 6 asymptotically approach the unperturbed Nusselt number as $f_j \to \infty$. This mirrors a similar observation made by Ilıcak and Vallis [14] from their simulations of horizontal convection perturbed by a sinusoidally time-varying shear across the heated boundary. They reported greater modification at larger amplitudes of forcing over their unstressed case, while the differences were more pronounced at the lower two frequencies they computed; their highest-frequency cases were similar to their unstressed case. They attributed this to the wind forcing having insufficient time at high frequencies to penetrate vertically into the flow before being cancelled by the shear reversal over each oscillation. The mechanism is similar in the present study: at any given jet amplitude, the vertical penetration of jet fluid into the enclosure decreases with increasing frequency (as it is governed by the integral of the jet velocity over half of the jet oscillation cycle, which vanishes in the limit as $f_j \to \infty$).

The appearance of two distinct local maxima at different frequencies is strongly suggestive of two unique modes of response being excited by the applied perturbation. To explore this further, the dependence of these modes on the amplitude of the synthetic jet perturbation is analysed, and subsequently visualisation of the disturbed flows is included.

The variation in the maximum Nusselt number for the LF and HF modes with jet amplitude is plotted in Fig. 7(a). While not obvious from Fig. 6, it is apparent that as amplitude is increased, both modes approach a common trend exhibiting an approximate scaling $\Delta Nu \sim A^{3/5}$, where $\Delta Nu = Nu - Nu_0$, and $Nu_0 = 8.1264$ is the Nusselt number of the unperturbed baseline case. This is interesting as it is suggestive of a common response being generated in the flow as a result of these two distinct forcing modes. The crossover amplitude between HF mode dominance and LF mode dominance is found to occur at $A_c \approx 75$. Fig. 7(b) plots the peak frequencies for the LF and HF modes. The HF mode exhibits a peak excitation frequency of $f_{j,pk} = 7.27 \times 10^3$ at low amplitudes ($A = \mathcal{O}(10^{-1})$), increasing slightly to $f_{j,pk} = 7.61 \times 10^3$ at $A \approx A_c$. The LF mode first increases from $f_{j,pk} = 3.76 \times 10^3$ at $A \approx 10$ to $f_{j,pk} = 4.14 \times 10^3$ at $A \approx 10^2$, before receding to $f_{j,pk} = 3.61 \times 10^3$ at $A \approx 10^3$. It is notable that the first harmonic of the LF mode aligns closely to $f_{j,pk}$ for the HF mode. In light of the collapse in ΔNu at higher jet amplitudes seen in Fig. 7(a), this suggests that both the LF and HF modes may be exciting a common instability mode in the flow, with a natural frequency in the HF mode waveband. It is recalled that Ilıcak and Vallis [14] reported that the addition of oscillatory shear stress to their heated boundary significantly modified their horizontal convection flows, with a deep eddying flow increasing in strength with increasing forcing strength. The section to follow will show that the synthetic jet perturbation invokes an unsteady end-wall plume, which has similarities to the unsteady eddying flow reported by Ref. [14]. To probe further, we select representative frequencies for the LF and HF mode wavebands of $f_{LF} = 4000$ and $f_{HF} = 7500$, respectively.

3.3. Temperature fields

A sequence of the temperature field for $A = 32$ and $f_j = 4000$ (LF

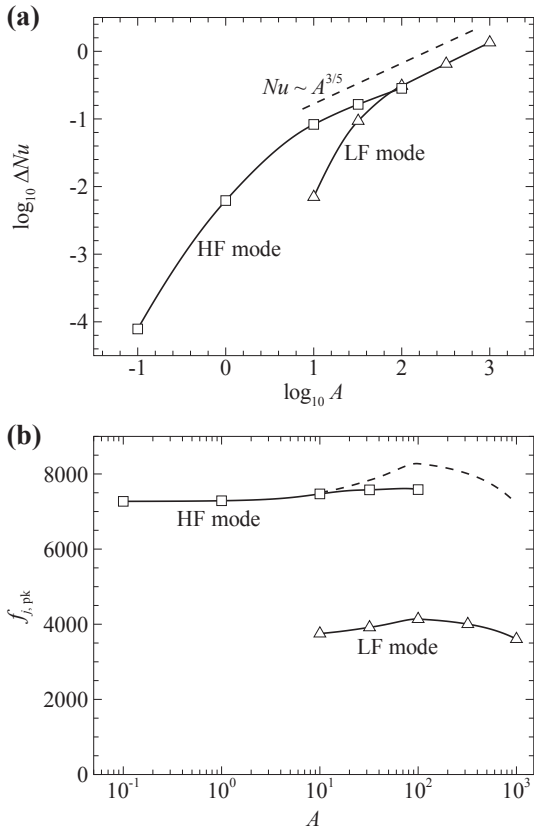

Fig. 7. (a) Logarithm of the increase in Nusselt number plotted against the logarithm of amplitude for the two modes of excitation, exhibiting an approximate scaling of $\Delta Nu \sim A^{3/5}$ (dashed line included for guidance) at higher amplitudes. (b) Frequencies of maximum Nusselt number plotted against jet amplitude. The dashed curve shows the frequency of the endwall plume disturbance excited by the HF mode perturbation.

mode) is shown in Fig. 8. The length of the sequence is one perturbation period. Comparing to the temperature field of the baseline case (Fig. 5), there was no visible differences in the left hand half of the enclosure, which is therefore omitted from these frames. The effects of the perturbation are evident in the right hand side of the domain, particularly in the boundary layer and in the vertical plume. Downstream of the synthetic jet (located at $x = 0.7L$) the boundary layer begins to oscillate and gives rise to unsteadiness within the plume the hot portion of the fluid (indicated in yellow) rises up the plume and begins to diffuse before it reaches the top, cooling into its surrounds and forming part of a diffuse return flow travelling to the left along the upper surface Fig. 8(a–c). While this is occurring, a second packet of hot fluid is advecting downstream in the boundary layer towards the plume. At approximately the halfway point of the sequence Fig. 8(e), this second packet of hot fluid begins to rise up in the plume. There are two ejections of hot fluid in the vertical plume per perturbation period. Furthermore, as the second ejection is occurring towards the end of the period Fig. 8(e–h) a new accumulation of hot fluid is building in the boundary layer for the next cycle. Arrows indicate the position of successive packets of hot fluid through the sequence shown in the figure.

A corresponding time sequence in the HF mode frequency band with synthetic jet properties $A = 32$ and $f_j = 7500$ is shown in Fig. 9. Similar features to the LF mode case are seen: an unsteady circulation forming beyond the perturbation, which continues to propagate downstream until the end wall is reached. The end wall plume transfers the destabilizing buoyancy to the top of the enclosure before it diffuses into the interior of the enclosure. As the plume ejects the instability a new packet of fluid begins to form as the new period begins. However, the key difference is that for the HF mode case a single ejection of a packet of buoyant fluid into the plume per perturbation cycle is seen, compared to the two ejections per cycle in the LF mode case. This points to both modes exciting a resonance that is naturally occurring within the flow.

A convective instability process is hinted by Fig. 9. Initially there is only a small ripple of increased hot fluid within the boundary layer (Fig. 9(a)), but as the sequence progresses (Fig. 9(c-g)) this feature convects to the right and enlarges, before breaking near the hot wall and convects upwards within the end-wall plume.

Hazewinkel et al. [15] reported at $Pr = 10$ evidence of a convectively unstable boundary layer leading to unsteady plumes penetrating vertically into the enclosure. Their mechanical forcing was applied indirectly as a uniform shear across the heated

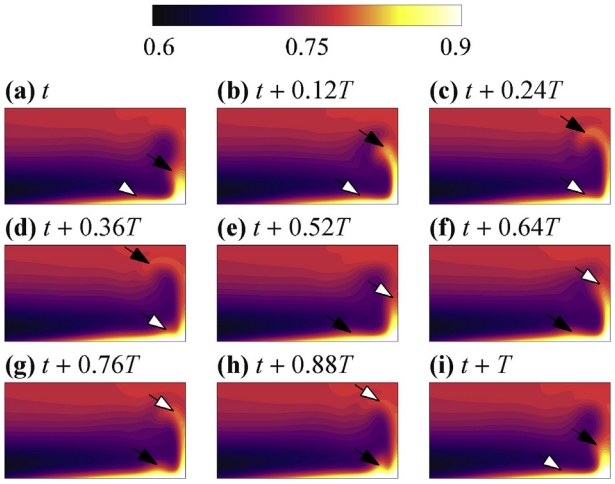

Fig. 8. Time sequence of the temperature field for a flow with synthetic jet properties $A = 32$ and $f_j = 4000$ (LF mode). The sequence is one perturbation period (T) in length. The area shown is the full height of the enclosure and $0.7L \le x \le L$. Dark and light shading denote cooler and hotter fluid ranging over $0.6 \le \theta \le 0.9$, respectively, and arrows identify disturbances convecting in the boundary layer that are ejected upward as buoyant eruptions in the end-wall plume. Two such eruptions are seen per perturbation period for the LF mode.

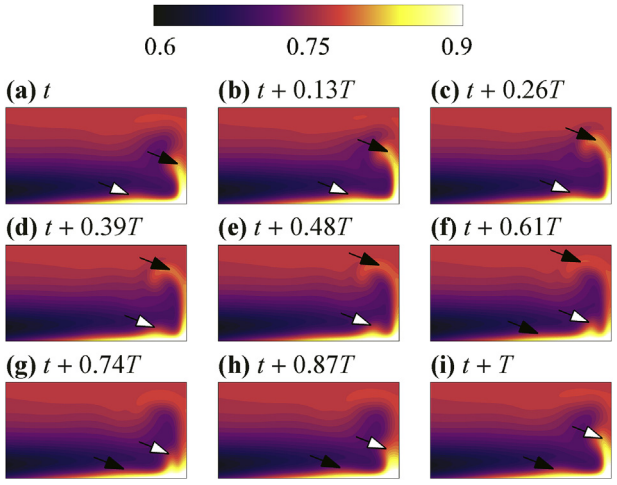

Fig. 9. Time sequence of the temperature field for a flow with synthetic jet properties $A = 32$ and $f_j = 7500$ (HF mode). The sequence is one perturbation period (T) in length. The area shown is the full height of the enclosure and $0.7L \le x \le L$. Shading and arrows are as per Fig. 8, but here only a single eruption is seen per perturbation period.

boundary, and they identified an intermediate regime of shear forcing that induced a sufficiently strong buoyancy inversion in the boundary layer to invoke an unsteady boundary layer convection. In general, their forcing invoked a shallow counter-rotating shear-driven cell over part of the heated boundary, with the thermally driven overturning cell occupying much of the remainder of the enclosure. Smaller shear forcing led to insufficient modification of the thermally driven overturning flow and no counter-rotating shallow cell formation, while excessive shear forcing produced a stable reversed flow over much of the base. Their buoyancy contour plots (ref. Fig. 3 in Ref. [15]) over these three regimes demonstrate that increasing indirect shear forcing progressively increases the inverted buoyancy gradient in the boundary layer. However, the increased shear forcing also widens the counter-rotating cell. In the context convective instability, a competition is therefore seen between the increasing strength of the buoyancy inversion promoting unstable boundary layer flow and the shrinking proportion of the forcing boundary layer over which the thermal overturning cell is in contact with the forcing boundary.

3.4. Frequency analysis

The discrete Fourier transform (DFT) of the $\mathscr{L}^2$ norm time history for the two dominant modes at $f_j = 4000$ and 7500 and $A = 32$ are shown in Fig. 10. The first harmonic occurs at the perturbation frequency for each case and subsequent harmonics occur at multiples of the perturbation frequency (i.e. f_j, $2f_j$,…,nf_j). Significantly more harmonics are observed for the LF mode disturbance ($n \approx 11$) than the HF mode ($n \approx 6$). The second harmonic of the LF mode is similar in magnitude to the first harmonic, while the harmonics of the HF mode case decay monotonically with increasing frequency. This second harmonic for the LF mode reveals a strong response in the flow that corresponds to a frequency that is approximately the same as the perturbation frequency for the HF mode. The LF mode is being perturbed at approximately half the frequency of the HF mode, but ultimately the end-wall plume emits vortices at a similar frequency to the HF mode. This agrees well with what is seen in the temperature flow fields and suggests that these two perturbation frequencies are exciting a natural frequency of the end wall plume at this Rayleigh number. This harmonic frequency is plotted along with the peak frequencies as a function of amplitude in Fig. 7(b), where the LF mode harmonic can be seen to align with the dominant frequency of the HF mode disturbance.

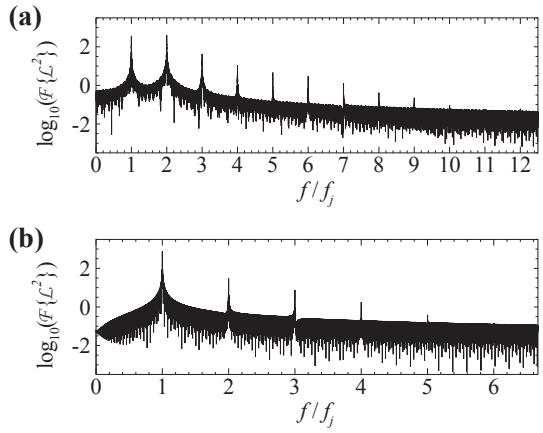

Fig. 10. Fast Fourier transform of the saturated $\mathscr{L}^2$ norm time history, plotted against normalised frequency (f/f_j). In both cases $A = 32$, while (a) and (b) depict jet frequencies $f_j = 4000$ and 7500, respectively. The domain of frequencies displayed in both frames is $0 \le f \le 5 \times 10^4$.

3.5. Disturbance field evolution

A clearer picture of the flow response to the applied perturbation emerges when isolating the disturbance. By subtracting the vorticity field of the baseline case from the vorticity field of the perturbed flow, the disturbance vorticity field is isolated. Time sequences of the disturbance field over a single period of the synthetic jet at $A = 32$ for the LF mode ($f_j = 4000$) and HF mode ($f_j = 7500$) are shown in Figs. 11 and 12, respectively. Both cases show similarities to Rayleigh–Bénard convection instability as evidenced by paired positive and negative vortices within the forcing boundary layer that grow in strength as they move towards the end wall. There they seed the ejection of eddies vertically upward into the end-wall plume. Considering the LF mode case, the strong positive vorticity region (indicated in red) in the lower right hand corner is transported up the right hand wall to the top of the enclosure before it is ejected towards the centre of the domain. Meanwhile, at approximately half the perturbation period, a second strong positive vortex begins to form, which follows the same sequence and is ejected from the end wall plume. In contrast, the HF mode transports one strong positive vortex through the end wall plume over the oscillation period. This demonstrates that the plume is shedding at the first harmonic frequency (8000) for the LF mode, and at the driving frequency (7500) for the HF mode. This is reflected in the DFT spectra in Fig. 10, where the LF mode exhibits approximately twice as many distinct harmonics. The jet disturbance is similar for both modes, suggesting that the different driving frequencies excite the same natural instability mechanism in the flow (manifesting in the end-wall plume).

Numerical simulations of horizontal convection driven by a linear temperature profile imposed along the bottom of a two-dimensional rectangular enclosure with an applied periodic perturbation have been carried out. These simulations demonstrate that a substantial increase in the Nusselt number over the non-perturbed case is exhibited over a large range of applied dimensionless perturbation frequencies ($0 < f_j \lesssim 10^4$). Two distinct peaks in Nusselt number occur, with properties suggesting a forced convection and natural convection mode.

Instabilities are evident in the forcing boundary layer that advect downstream and lead to ejection of eddies in the end wall plume and vortex pairs forming. Instability that is observed as

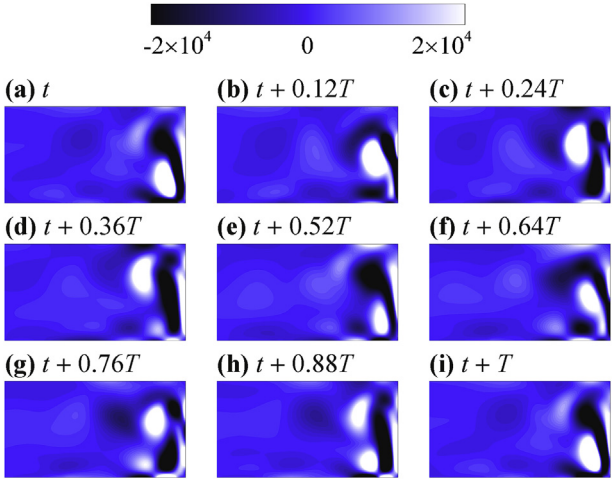

Fig. 11. Time sequence of the disturbance vorticity field for a perturbation amplitude of 32 and frequency of 4000 (LF mode). The area shown is the full height of the enclosure and $0.7L \le x \le L$. Dark and light shading respectively shows negative and positive disturbance vorticity over $-2 \times 10^4 \le \omega_z \le 2 \times 10^4$, respectively, and the sequence is one perturbation period in length.

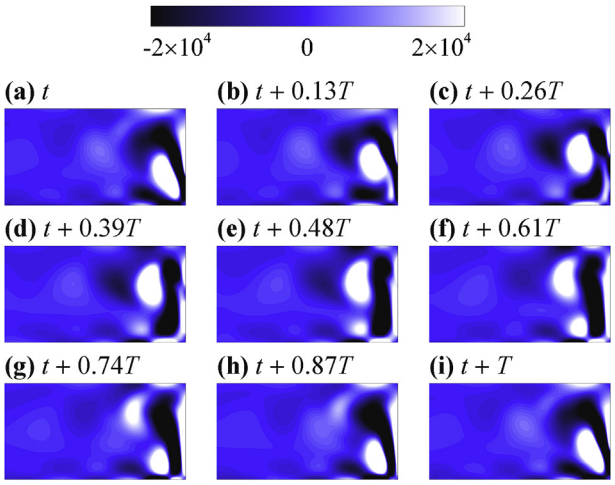

Fig. 12. Time sequence of the disturbance vorticity field for a perturbation amplitude of 32 and frequency of 7500 (HF mode). Frames and shading are as per Fig. 11.

unsteadiness in the vertical plume actually originates as convectively unstable waves travelling in the forcing boundary layer, as demonstrated in the disturbance fields, which show a distinct vortex structure that convects to the right from the point of disturbance in the boundary layer.

Furthermore, the instability structure is consistent with Rayleigh–Bénard convection. Rayleigh–Bénard convection occurs when a fluid is heated strongly from below, which is exactly what is happening in the thermal boundary layer at the hotter end of this horizontal convective flow. Hot buoyant fluid lies below cooler denser fluid seeking to fall, which creates convection cells of a Rayleigh–Bénard type. The vorticity field generated by Rayleigh–Bénard convection comprises a horizontal array of alternating-sign vortices above the heated surface, each of which is adjacent to a zone of opposite-signed vorticity attached to the surface. This is very similar to the instability structure seen in the disturbance vorticity fields towards the hot end of the bottom boundary.

It is emphasized that the horizontal convection flow is not globally absolutely unstable to infinitesimal perturbations at these Rayleigh numbers, but rather as Tsai et al. [19] demonstrate, the boundary layer profiles in horizontal convection are locally unstable (at least over part of the heated boundary and beyond a sufficient Rayleigh number). In other regions the overturning horizontal convection flow is stabilising, including the upstream boundary layer towards the cooler end and the slow return flow. Hence a finite extent of convectively unstable boundary layer appears to be required to provide a sufficient amplification to disturbances to support a self-sustaining instability in the flow. Presumably these disturbances decay as they are advected in the return flow before re-entering the boundary layer where they are re-amplified. If the growth rates and/or breadth of the locally unstable part of the boundary layer are too small, the stabilising parts of the overturning flow suppress the net growth of instability. Hazewinkel et al.s [15] higher-Prandtl-number work (their Fig. 3(b,c)) shows a similar behaviour, where horizontal convection with opposing surface stress manifests a region of strong inverted buoyancy at the downstream end of the horizontal convection boundary layer. In their Fig. 3(b), unstable flow emerges from the horizontal convection boundary layer, but not in their Fig. 3(c): a notable difference between the two cases is the significantly shorter length of boundary layer available to amplify disturbances seen in their Fig. 3(c) compared to their Fig. 3(b).

By independently controlling the frequency and amplitude of the disturbance it was seen that excitation in the flow is realised using a range of perturbation frequencies. However, the two dominant frequency wave bands invoke the same instability in the flow, which is strongly suggestive of the flow having a natural dominant instability mode that can be initiated in different ways and is not dependent on the perturbation mechanism. Despite being driven by two perturbation frequencies that differ by a factor of approximately two, ultimately both of these resultant modes are a consequence of exciting the same natural frequency in the plume, which at $Ra = 2.5 \times 10^8$ and $Pr = 6.14$ is approximately 7500.

In the steady-state regime, heat transport has been shown to be independent of H/L down to a Rayleigh number corresponding to the point at which the boundary layer has become sufficiently thick that it is affected by the confinement of the opposite boundary [5]. For steady-state flows, the scaling of boundary layer thickness with Rayleigh number determines the transition between diffusion-dominated flows at lower Rayleigh numbers and horizontal convection with a distinct boundary layer at higher Rayleigh numbers. The onset of unsteady flow has been shown to be independent of H/L at least for aspect ratios typical of those considered in the majority of published experimental and laboratory studies into horizontal convection, i.e. $H/L \geq 0.16$. Presumably, below some H/L the critical Rayleigh number will similarly be affected by the shallow-enclosure confinement. If unsteady flow was solely a determined by, and manifested within, the unstable boundary layer, then its onset would be expected to be limited by Rossbys scaling for the boundary layer thickness at small H/L. However, given that the present study demonstrates that the unsteady-flow state is determined in part by the end-wall plume, then confinement of the plume, rather than the boundary layer, will presumably control the limiting depth below which the critical Rayleigh number becomes dependent on H/L. Chiu-Webster et al. [36] describe that the end-wall plume is driven by buoyancy near the heated boundary, but becomes a momentum jet further from the boundary. As the plume penetrates significantly deeper into the enclosure than the boundary layer, this effect will emerge at larger H/L than expected based on the scaling of the boundary layer with Rayleigh number alone. This may then carry implications for the quantification of the contribution of the horizontal convection mechanism to horizontal heat transport in Earth's oceans, where despite the Rayleigh numbers being very high (possibly $\mathscr{O}(Ra^{30})$ or more [16]), the height ratios are very small ($H/L < \mathscr{O}(0.001)$).

4. Conclusions

A synthetic jet embedded within the boundary layer of a horizontal convection flow is found to excite two modes of excitation, which produce an increase in Nusselt number. With increasing jet amplitude, both modes approach a single trend for the peak Nusselt number that goes with the 3/5 th power of the amplitude. At small amplitudes, a higher-frequency mode with dimensionless frequency $f_j \approx 7.5 \times 10^3$ dominates, whereas at larger amplitudes a lower-frequency mode with $f_j \approx 4 \times 10^3$ dominates. Interrogation of thermal fields and disturbance vorticity reveals that the jet invokes a boundary-layer disturbances with a structure consistent with a Rayleigh–Bénard type of thermal instability. These disturbances convect towards the enclosure end-wall with frequencies matching the respective applied perturbations. However, both modes produce an oscillation in the vertical plume at the end-wall having a frequency consistent with the high-frequency mode: A common instability response in the end-wall plume is incited by *different* upstream perturbations. It then follows that the emergence of time-periodic unstable flow beyond the critical Rayleigh number in horizontal convection may be due to a natural instability

of the end-wall plume that controls the frequency of the oscillation in the flow, and is excited by upstream disturbances—the source of these disturbances is the amplifying effect of the convectively unstable thermal boundary layer at Rayleigh numbers $Ra > \mathcal{O}(10^8)$.

Acknowledgments

This project is supported by the Australian Research Council through Discovery Grants DP120100153 and DP150102920. Numerical simulations were facilitated by a high-performance computing time allocation from the National Computational Infrastructure (NCI) Merit Allocation Scheme, and access to the Monash SunGRID thanks to the Monash e-Research Centre. NCI is supported by the Australian Government.

References

[1] Hughes GO, Griffiths RW. Horizontal convection. Annu Rev Fluid Mech 2008;40:185–208.
[2] Beardsley RC, Festa JF. A numerical model of convection driven by a surface stress and non-uniform horizontal heating. J Phys Oceanogr 1972;2:444–55.
[3] Mullarney JC, Griffiths RW, Hughes GO. Convection driven by differential heating at a horizontal boundary. J Fluid Mech 2004;516:181–209.
[4] Hughes G, Griffiths R, Mullarney J, Peterson W. A theoretical model for horizontal convection at high rayleigh number. J Fluid Mech 2007;581:251–76.
[5] Sheard GJ, King MP. Horizontal convection: effect of aspect ratio on Rayleigh number scaling and stability. Appl Math Model 2011;35:1647–55.
[6] Gayen B, Griffiths RW, Hughes GO, Saenz JA. Energetics of horizontal convection. J Fluid Mech 2013;716:R10.
[7] Barkan R, Winters KB, Llewellyn Smith SG. Rotating horizontal convection. J Fluid Mech 2013;723:556–86.
[8] Gayen B, Griffiths RW, Hughes GO. Stability, transitions and turbulence in horizontal convection. J Fluid Mech 2014;751:698–724.
[9] Hussam WK, Tsai TK, Sheard GJ. The effect of rotation on radial horizontal convection and Nusselt number scaling in a cylindrical container. Int J Heat Mass Trans 2014;77:46–59.
[10] Paparella F, Young WR. Horizontal convection is non-turbulent. J Fluid Mech 2002;466:205–14.
[11] Scotti A, White B. Is horizontal convection really “non-turbulent?”. Geophys Res Lett 2011;38. L21609.
[12] H. T. Rossby, On thermal convection driven by non-uniform heating from below: an experimental study, in: Deep sea research and oceanographic abstracts, vol. 12, Elsevier, pp. 9–16.
[13] Wang W, Huang RX. An experimental study on thermal circulation driven by horizontal differential heating. J Fluid Mech 2005;540:49–73.
[14] Ilıcak M, Vallis GK. Simulations and scaling of horizontal convection. Tellus A 2012;64:18377.
[15] Hazewinkel J, Paparella F, Young WR. Stressed horizontal convection. J Fluid Mech 2012;692:317–31.
[16] Siggers J, Kerswell R, Balmforth N. Bounds on horizontal convection. J Fluid Mech 2004;517:55–70.
[17] Grossmann S, Lohse D. Scaling in thermal convection: a unifying theory. J Fluid Mech 2000;407:27–56.
[18] Shishkina O, Grossmann S, Lohse D. Heat and momentum transport scalings in horizontal convection. Geophys Rev Lett 2016;43(3):1219–25. http://dx.doi.org/10.1002/2015GL067003.
[19] Tsai T, Hussam WK, Fouras A, Sheard GJ. The origin of instability in enclosed horizontally driven convection. Int J Heat Mass Trans 2016;94:509–15.
[20] Schubauer GB, Skramstad HK. Laminar-boundary-layer oscillations and transition on a flat plate. NACA Rep 1948;909:327–57.
[21] Glezer A, Amitay M. Synthetic jets. Annu Rev Fluid Mech 2002;34:503–29.
[22] Walther S, Airiau C, Bottaro A. Optimal control of Tollmien–Schlichting waves in a developing boundary layer. Phys Fluids 2001;13:2087–96.
[23] Cattafesta I, Louis N, Sheplak M. Actuators for active flow control. Annu Rev Fluid Mech 2011;43:247–72.
[24] Dandois J, Garnier E, Sagaut P. Numerical simulation of active separation control by a synthetic jet. J Fluid Mech 2007;574:25–58.
[25] Moarref R, Jovanović MR. Controlling the onset of turbulence by streamwise travelling waves. part 1. receptivity analysis. J Fluid Mech 2010;663:70–99.
[26] Lieu BK, Moarref R, Jovanović MR. Controlling the onset of turbulence by streamwise travelling waves. part 2. direct numerical simulation. J Fluid Mech 2010;663:100–19.
[27] Sandstrom JW. Dynamische versuche mit meerwasser. Ann Hydrogr Mar Met. 1908;36:6–23.
[28] Tailleux R, Rouleau L. The effect of mechanical stirring on horizontal convection. Tellus A 2010;62:138–53.
[29] Tsai TK, Hussam WK, Sheard GJ. Global and convective stability of horizontal convection. In: Chowdhury H, Alam F, editors. The proceedings of the 19th australasian fluid mechanics conferece. Australasian Fluid Mechanics Society; 2014. Paper 108, ISBN: 978-0-646-59695-2.
[30] Hamid AHA, Hussam WK, Pothérat A, Sheard GJ. Spatial evolution of a quasi-two-dimensional Kármán vortex street subjected to a strong uniform magnetic field. Phys Fluids 2015;27:053602.
[31] Sheard GJ, Hussam WK, Tsai T. Linear stability and energetics of rotating radial horizontal convection. J Fluid Mech 2016;795:16–35.
[32] Karniadakis GE, Sherwin SJ. Spectral/hp element methods for computational fluid dynamics. Oxford University Press; 2005.
[33] Karniadakis GE, Israeli M, Orszag SA. High-order splitting methods for the incompressible Navier–Stokes equations. J Comput Phys 1991;97:414–43.
[34] Rønquist EM. Convection treatment using spectral elements of different order. Int J Numer Meth Fl 1996;22:241–64.
[35] Blackburn HM, Sherwin SJ. Formulation of a Galerkin spectral element–Fourier method for three-dimensional incompressible flows in cylindrical geometries. J Comput Phys 2004;197:759–78.
[36] Chiu-Webster S, Hinch EJ, Lister JR. Very viscous horizontal convection. J Fluid Mech 2008;611:395–426.